Journal of Vibration and Control
http://jvc.sagepub.com/

Dynamic modeling of electromagnetic suspension system

Nam H Kim and Long Ge

Journal of Vibration and Control published online 21 February 2012
DOI: 10.1177/1077546312438601

Article

JVC

Journal of Vibration and Control
0(0) 1–13

DOI: 10.1177/1077546312438601
jvc.sagepub.com
SAGE

Dynamic modeling of electromagnetic suspension system

Nam H Kim and Long Ge

Abstract

Characteristics of magnetic-levitation systems are studied using dynamic models that include motion-dependent lift, drag, slip, and roll motions. The contact constraint between the vehicle and the track is modeled using a compliant contact model, and inelastic restitution is modeled using damping. Unknown numerical parameters are identified using an optimization technique and experimental data. The numerical tests are focused on the damping characteristics, stability in lifting and slip motions, the lifting efficiency, and the contact behavior with the track. It turns out that the suspension system does not have any inherent damping in the lifting direction. However, a stable behavior is observed in the traveling direction. The model also shows that the system has a strong concentric force that stabilizes the vehicle in the slip motion as well as in the rolling motion.

Keywords

Dynamic model, magnetic levitation, suspension, contact, regression

Received: 30 April 2009; accepted: 10 July 2011

1. Introduction

The maglev (magnetic-levitation) system utilizes magnetic fields produced from ground based electrical power sources to levitate a vehicle above the track. The vehicle is then accelerated along the track using high-power electromagnets (Powell and Danby, 1971; Luerkin, 1994; Kalsi, 1994; Rote and Cai, 2002). Recently, Post and Ryutov (1996, 2000) proposed a new concept, Inductrack, that provides a passive means of levitation. The realization of a stabilized ride using maglev has been a major hurdle in developing its feasibility for this purpose. The main scope of this paper is to examine the feasibility of the Inductrack magnetic-levitation system, developed at the Lawrence Livermore National Laboratory, by identifying the dynamic characteristics of the magnetic-levitation suspension system with computational dynamic analysis.

The maglev system is composed of a vehicle (cradle) with permanent magnets and a rail with coils in it. The magnets and the coils produce an electromagnetic field, and once the cradle starts moving, the change in the magnetic field results in an electromagnetic force. A moving cradle with a special configuration of high-strength permanent magnets generates passive magnetic levitation when it moves over multi-loops of wire embedded in the track underneath. This system is configured so that the resulting electromagnetic forces are decomposed into driving forces and lifting forces. Compared with other maglev systems, the Inductrack system can provide levitation forces with simpler and less expensive equipment.

The early stages of development of the maglev system have focused on how to generate enough lifting force using a special array of magnets. It has been demonstrated by Post and Ryutov (2000) that the Inductrack concept can be used to build a simpler and less expensive system using a Halbach array (Halbach, 1985) of permanent magnets, which induces repelling currents in a close-packed array of shorted conducting circuits in the track. Basing their study on lumped-circuit analysis, they showed that the maximum

Department of Mechanical and Aerospace Engineering, University of Florida, USA

Corresponding author:
Nam H Kim, Department of Mechanical and Aerospace Engineering, University of Florida, Gainesville, FL 32611, USA
Email: nkim@ufl.edu

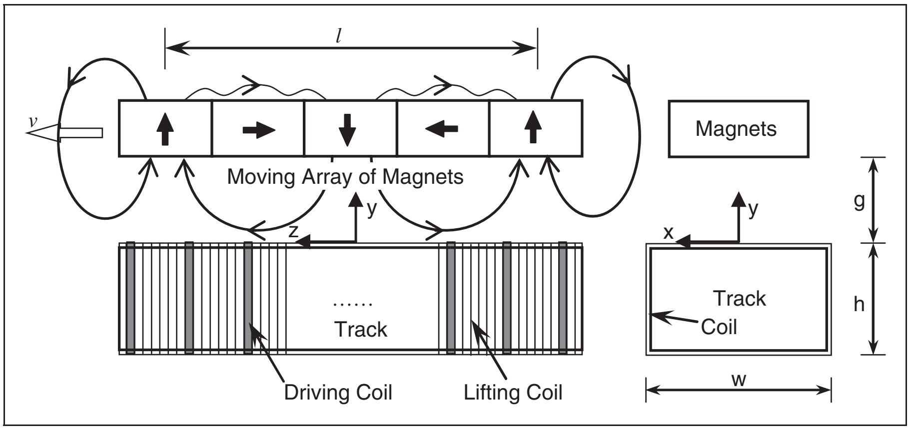

Figure 1. Passive magnetic levitation using a Halbach array of magnets. The horizontally polarized magnets concentrate the flux on one side of the array and help to form the sinusoidal flux shape. Driving coils generate synchronous pulses to provide thrust in the z-direction.

levitation capacity was up to 40 tons per square meter of magnets. As shown in Figure 1, permanent magnets with a direction of magnetization that is rotated by 90° with respect to adjacent magnets produce a sinusoidal variation of a magnetic field at a constant distance from the bottom of the array. This array maximizes the magnetic field below the array, while cancelling out the field above it. When the array of magnets moves over the inductively loaded circuit track, the track induces repelling currents that levitate the magnet, or the cradle attached to it. Conceptually the system is stable because the levitation force is only generated when the cradle is moving and it settles on the track when the speed is reduced below a threshold.

However, the practical application of the maglev system requires stability and reliability of the system under various operating conditions (Matsue et al., 2001; Boeij et al., 2005). Motion-based magnetic forces are important because they can induce various types of instability in the maglev system (Dill and Meeker, 2000). In addition, the periodic structure of the magnetic forces may also induce parametric and combination resonances, especially because the lifting force is inversely proportional to the exponential distance between the permanent magnet and the track. A small perturbation of the cradle position can cause a large variation in the lifting force, which is then related to the stability and ride quality of the system. Thus, it is essential to model the dynamic system when the body force field is coupled with the kinematics of the system.

In this paper, a new dynamic system modeling technique is proposed to consider the highly nonlinear effect of the electromagnetic force field that is changed in the pattern of the sinusoidal wave along the track. The coupled mechanical and magnetic system is governed by a nonlinear system of differential equations. The dynamic behavior of the mechanical system depends on the force generated by the magnetic field, while the magnetic force depends on the location and velocity of the structure.

2. Review of magnetic suspension system modeling

2.1. Magnetic suspension modeling

The theoretical study of the magnetic levitation force has been performed in depth by Post and Ryutov (2000) using the lumped-circuit analysis. In this section, the theory of the magnetic suspension that can be used in the dynamic analysis in the following sections is presented.

Consider a Halbach array of magnets, as shown in Figure 1, with width w, wavelength λ, and peak strength B_0 of the magnetic field at the surface. The cradle is attached on top of the magnets, and the coils are winded on the outer surface of the window-frame track. The coordinate system is established such that the origin is on the top surface of the track, the cradle is traveling in the z-coordinate direction, and it is levitated in the y-coordinate direction. Let the array be moving in the z-direction with velocity v_z, and the gap between the bottom surface of the magnets and the coils be g. The wave number of the Halbach array is $k = 2\pi/\lambda$, and the angular frequency of the magnetic field due to the motion of the cradle is $\omega = kv_z$. Then, the magnetic field from the array can be approximated by

$$\begin{aligned} B_z(y) &= B_0 \sin(\omega t) e^{-k(g-y)} \\ B_y(y) &= B_0 \cos(\omega t) e^{-k(g-y)} \end{aligned} \tag{1}$$

where $B_z(y)$ and $B_y(y)$ are, respectively, the longitudinal and vertical components of the magnetic field at the distance y from the coils. The magnetic field is an exponential function of distance y and shows a sinusoidal behavior as it moves along the track. With the strength of $B_0 = 1.0$ Tesla, for example, a square-meter-sized magnet can levitate about 40,000 kg (Post and Ryutov, 1996).

From the assumption that the coils in the track have negligible thickness, the induced flux can be obtained by integrating B_z over the upper and lower legs of the coils, as

$$\phi = \phi_0 \sin(\omega t) = \frac{wB_0}{k}\exp(-kg)\sin(\omega t), \tag{2}$$

where ϕ_0 is the peak flux enclosed by the circuit, which depends on the gap g. The contribution from the coils in the lower legs is ignored in Equation (2) because their contribution is less than 0.2% when the height of the track is the same as the wavelength of the magnets.

The moving magnets over the closed circuit induce currents, which are governed by the following circuit equation:

$$L\frac{dI}{dt} + RI = \omega\phi_0\cos(\omega t), \tag{3}$$

where $I(t)$ is the induced current, L the inductance, and R the resistance of the circuit. The flux varies with $\sin(\omega t)$, and the voltage is proportional to the rate of change of the flux through the circuit. The induced current in the steady-state can be obtained by solving Equation (3) as

$$I(t) = \frac{\phi_0}{L}\frac{1}{1+(R/\omega L)^2}\left[\sin(\omega t) + \frac{R}{\omega L}\cos(\omega t)\right], \tag{4}$$

where the peak flux ϕ_0 is available from Eq. (2).

The induced current interacts with the magnetic field to produce the following levitation (lift) and drag forces:

$$\begin{aligned} F_{\text{lift}} &= IB_z w \\ F_{\text{drag}} &= IB_y w, \end{aligned} \tag{5}$$

where w is the width of the magnets. As the speed of the cradle increases, the ratio $R/\omega L$ becomes smaller. In such a case, the $\cos(\omega t)$ term in Equation (4) can be negligible, and the induced current $I(t)$ is in phase with the flux $B_z(t)$ in Equation (1), which yields the maximum levitation force. The forces in Equation (5) vary along the wavelength of the magnets. Using the relation of $\omega t = kz$ and averaging Equation (5) over the wavelength of the magnets, the averaged levitation and drag forces, respectively, can be obtained as

$$\langle F_{\text{lift}}(v,g)\rangle = \frac{B_0^2 w^2}{2kL}\frac{1}{1+(R/\omega L)^2}e^{-2kg}, \tag{6}$$

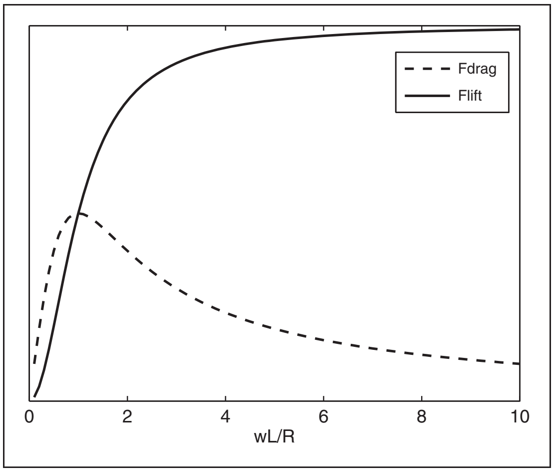

Figure 2. The normalized levitation and drag forces as a function of speed.
Note that the drag force reduces after the transition speed $w = R/L$.

$$\langle F_{\text{drag}}(v,g)\rangle = \frac{B_0^2 w^2}{2kL}\frac{(R/\omega L)}{1+(R/\omega L)^2}e^{-2kg}. \tag{7}$$

These forces are exerted by a single circuit. In the following derivations, all forces are averaged over the wavelength of the array, and the angled brackets < > will be dropped for notational simplicity.

The efficiency of the magnetic suspension system is often measured as the life/drag ratio. From Equations (6) and (7), this ratio becomes

$$\frac{F_{\text{lift}}}{F_{\text{drag}}} = \frac{\omega L}{R} = \frac{2\pi v_z}{\lambda}\frac{L}{R}. \tag{8}$$

As the velocity increases, the ratio increases linearly; thus, the system becomes more efficient at high velocity. For the estimated operating velocity of the cradle (40 m/s), the ratio can reach up to 200 : 1. Figure 2 shows the normalized levitation and drag forces as a function of the ratio $\omega L/R$. The levitation force, F_{lift}, increases quickly at low speed and eventually converges to its maximum value, while the drag force, F_{drag}, reaches its maximum value at the transition velocity $\omega = R/L$ and then reduces gradually. Note that the maximum value of the drag is half of the maximum levitation force.

The magnetic suspension model described in Equations (6) and (7) has several distinguished characteristics compared to the traditional spring–damper suspension system. First, the levitation force is an exponential function of the gap g. It can be considered as a nonlinear spring. It also depends on the velocity of the cradle. When the velocity is increased above a threshold, the moving magnet array induces enough currents in the coils and thereby levitates the cradle. On the other hand, when the driving force is less than the drag force, the cradle simply slows down and comes to rest on the track using auxiliary wheels. Second, there is no damping mechanism in the suspension system. This characteristic has not been discussed in the literature, but it is very important to the stability of the system. Based on linear perturbation theory, Post and Ryutov (1996) showed that the magnetic suspension system has negative damping, even if its magnitude is reduced as the velocity increases. If a fluctuation occurs due to a flaw in the coils or an external excitation, the cradle will vibrate continuously. The only available damping is from the aerodynamic drag and structural damping, whose effect was not studied previously.

2.2. Thrust mechanism

Even if the levitation can be achieved without requiring external power sources, it is always accompanied with the unwanted drag force, as can be seen in Equation (8). In order to overcome the drag, an external thrust force must be provided to the system. In practice, driving coils are implemented between lifting coils in the track, so that impulsive currents are provided according to the position of the cradle to produce the thrust force (see Figure 1). In order to achieve the maximum thrust, the impulsive current is provided when the peak of the magnetic field B_y is present. From Equation (1), the peak of B_y occurs when the position of the magnets is an integer times the wavelength, i.e. $z = n\lambda$, where n is a positive integer. At that location, the maximum magnetic field becomes

$$B_{y,\max} = B_0 e^{-kg}. \tag{9}$$

When the magnetic field reaches its maximum value in the position of the driving coil, an impulsive current I_D is provided to generate a thrust force to the magnets. The peak of the thrust force from the circuit, which depends on the drive current, is given by

$$F_p = I_D B_{y,\max} w. \tag{10}$$

When the drive current is delivered in half sine-wave pulses with a pulse length of τ, the incremental moment per pulse can be found by integrating the thrust force over the pulse length, as

$$m\Delta v = F_p \int_0^\tau \sin\left(\frac{\pi t}{\tau}\right) dt = F_p \frac{\tau}{\pi}. \tag{11}$$

For the given Halbach array in Figure 1, the pulse of the current can be provided at every half-wavelength. Thus, the frequency of the pulse is

$$f_p = 2v/\lambda. \tag{12}$$

Then, the averaged thrust force F_{drive} over the wavelength of the array becomes

$$F_{\text{drive}} = f_p m \Delta v = \frac{2v}{\lambda}\frac{\tau}{\pi} I_D B_0 e^{-kg} w. \tag{13}$$

The thrust force increases proportionally to the velocity of the cradle. However, the length of the pulse τ needs to be decreased at high velocity. The above thrust force can also be used to decelerate the cradle.

2.3. Aerodynamic drag

As the cradle moves with a high speed, the drag force caused by air can affect the motion of the cradle. This drag force is different from that of magnetic drag described in Equation (7). It is necessary to compare the magnitude of this drag force with the drag force caused by magnetic levitation in the previous section. The Reynolds number is first defined as

$$\mathrm{Re} = \frac{\rho v l}{\mu}, \tag{14}$$

where ρ is the density of the fluid, l the length of the cradle, and μ the absolute viscosity. For standard air at room temperature, the following data can be used: $\rho = 1.29\ \mathrm{kg/m^3}$ and $\mu = 1.862 \times 10^{-5}\ \mathrm{kg/m \cdot s}$. When the cradle is moving with a velocity of 40 m/s, the Reynolds number is larger than 10^6. Thus, it is assumed that the flow condition is turbulent and the following drag coefficient is used:

$$C_F = \frac{0.455}{(\log_{10} \mathrm{Re})^{2.58}}. \tag{15}$$

The drag force can be obtained by

$$F_D = C_F\left(\frac{1}{2}\rho V^2\right)(S_{\text{wetted}}) \tag{16}$$

Based on the current speed and geometry of the cradle, the expected drag force is about 2.5 N. Considering that each Halbach array can produce levitation and drag forces larger than 1000 N, the contribution from the aerodynamic drag force can be negligible.

In addition to the drag force, the pressure force can affect the dynamic behavior of the cradle. In the longitudinal direction, the cradle can be approximated by a thin plate. Thus, the pressure difference between the front and rear surfaces can be ignored. In the levitation direction, the cradle can be considered as a bluff body, which produces a large pressure difference. However, the velocity in the longitudinal direction is less than

0.1 m/s for the expected operating condition. In addition, the motion of the cradle is oscillatory. Thus, the effect of the pressure force can also be ignored in the levitation direction.

3. Dynamic models of a maglev system

3.1. Inductrack model

Even if the magnetic suspension model in the previous section shows the feasibility of passive levitation, a practical system needs to consider various situations including stability, ride–control, etc. A small-scale Inductrack model has been built by Lawrence Livermore National Laboratory, sponsored by NASA, with a 20-meter long track and a cradle of 9.3 kg, as shown in Figure 3. The proof-of-the-concept cradle includes six Halbach arrays, and each array is composed of five NdFeB magnets with 1 cm thickness, as shown in Figure 1. Three arrays are positioned in the front and the other three in the rear. The width of the arrays on the top is 12 cm, while the arrays on the side have a width of 8 cm. The role of the array on the top is mainly to provide levitation force, while the two arrays on the side provide stability through the strong concentric force. However, the levitation forces are compensated between top and side magnets, whereas the drag forces are accumulated for both magnets. This unexpected effect was not discussed in the original report because the theory is based on the flat magnets over the window-frame track. The properties of the permanent magnets are summarized in Table 1.

The 20-meter long track is built on top of the steel box beam, and coils are wound on the track. A coil assembly consists of 13 turns of levitation coils and one turn of driving coil. The levitation coil is made of a #10 square insulated magnetic wire and the drive coil is made of a #6 square insulated magnet wire. The thickness of the coil assembly is 5 cm. The track detects the position of the cradle using photo diode detectors and triggers the drive coil to produce a pulse of 7 kA current during a 600 μs time period. Since the magnetic field B_y changes its sign, the direction of current must switch to provide a forward thrust force. The parameters of the drive coil are also summarized in Table 1.

The cradle is 65 cm long and is made of carbon-fiber composite material. The weight of the cradle is 3.8 kg without magnets and 9.3 kg with magnets. Four auxiliary wheels are attached at the lower corners of the cradle in order to provide smooth landing when the speed is reduced below the threshold and to prevent the magnet from touching the coils.

In addition to the thrust force from the drive coil, a mechanical launcher is used to generate the initial speed. The mechanical launcher consists of six bungee cords and an aluminum sliding cage. The current design can generate an initial velocity of 9 m/s.

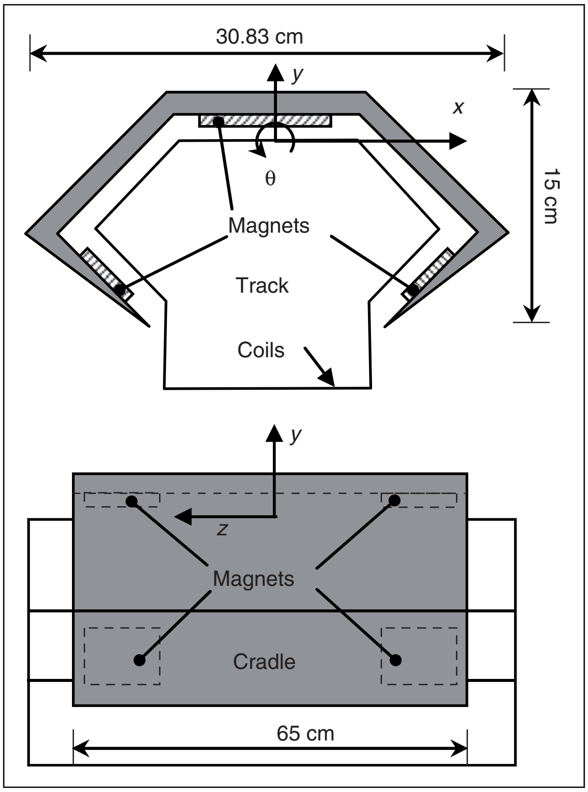

Figure 3. Inductrack proof-of-concept model. Six magnet arrays are located in the front and rear. The two top arrays provide the lift force, while four side arrays provide concentric force.

3.2. One-degree-of-freedom model

For most mechanical systems, the force is prescribed as a function of time. However, in the Inductrack system the magnetic force depends on the position and motion of the cradle. From the modeling perspective, this is equivalent to adding a nonlinear spring. The only difference is that the stiffness of the spring is not only a function of the position, but also a function of the motion. Using this analogy, an exponentially varying nonlinear spring can be attached to the bottom of the permanent magnets. However, this spring component needs to be modeled carefully, since the force changes according to the motion and location of the cradle.

As a first numerical study, a one-degree-of-freedom (1-DOF) model is considered. The cradle is modeled as a lumped mass and it is only allowed to move in the vertical direction. The longitudinal speed v_z of the cradle is assumed to be constant. Even if this model is the simplest one, the fundamental characteristics of the model, such as damping property and stability, can be obtained.

Table 1. Parameters of the Inductrack system

Parameter	Value	Note
B_0	0.52 T	Amplitude of the magnetic field
k	$k = 2\pi/\lambda = 20\pi$	Wave number of the Halbach Array
L	1.8×10^{-6} H	Lumped self-inductance
R	$1.5 \times 10^{-3}\,\Omega$	Resistance of the single circuit of track
ω	$\omega = kv = 20\pi v$	Frequency of the magnetic field variations
m	9.3 kg	Mass of the cradle
λ	0.1 m	Wave length
τ	600 μs	Impulse length
I_D	7000 A	Drive current
N_c	13	Number of lifting coil per wavelength
w_{top}	12 cm	Width of magnet array on the top
w_{side}	8 cm	Width of magnet array on the side

Let the gap between the top magnets and coils be g_1 and the gap between side magnets and coils be g_2. Since only vertical motion is allowed, these two gaps have the following relation: $g_2 = g_0 - (g_1 - g_0)\cos 45°$, where g_0 is the initial gap for all three magnets. When these three magnets move along the track, they induce the flux in the coils. The induced flux in Equation (2) comes from the assumption that the flat magnets move over the box-frame track that has the same width as the magnets. Since the track geometry of the Inductrack model is not a box shape and the magnets are not a single piece, however, Equation (2) cannot be used directly. In order to consider the effect of non-regular track geometry, a shape parameter α is introduced to express the peak flux, as

$$\phi_0 = \frac{\alpha B_0}{k}\left(w_{\text{top}}e^{-kg_1} + 2w_{\text{side}}e^{-kg_2}\right). \tag{17}$$

In the following section, an optimization technique will be employed to identify the shape parameter by comparing the simulation results with those from the experiment.

For the cradle model described in the previous section, the averaged levitation force can be written as

$$F_{\text{lift}}(v_z, g_1) = 2N_c\frac{B_0\phi_0}{2L}\frac{1}{1+(R/\omega L)^2} \times \left[w_{\text{top}}e^{-kg_1} - \sqrt{2}w_{\text{side}}e^{-kg_2}\right]. \tag{18}$$

The scalar value $2N_c$ is multiplied because there are N_c lifting coils in the wavelength of the magnets and two sets of arrays, one in front and the other in rear. The arrays on the top produce a positive levitation force, while the arrays on the side reduce it. In the case of the one-DOF model, the longitudinal speed is fixed; thus, only g_1 is a variable.

Using the levitation force in Equation (18), the second-order ordinary differential equation (ODE) can be written as

$$ma_y = F_{\text{lift}}(v_z, g_1) - ma_g, \tag{19}$$

where a_g is the gravitational acceleration that is applied to the negative y-coordinate direction. Aerodynamic damping is not considered. The above second-order ODE is converted to a system of first-order ODEs, as

$$\dot{\mathbf{q}} = \begin{Bmatrix} \dot{y}_1 \\ \dot{v}_y \end{Bmatrix} = \begin{Bmatrix} v_y \\ F_{\text{lift}}/m - a_g \end{Bmatrix}, \tag{20}$$

where the generalized coordinate is defined as $\mathbf{q} = \{y_1, v_y\}^{\text{T}}$. The initial condition is given as $\mathbf{q}_0 = \{1\text{cm},\ 0\}^{\text{T}}$, i.e. the initial gap is 1 cm.

The above ODE is solved using the ‘ode15s ’ function in MATLAB, which uses a variable order solver based on numerical differentiation formulas. When the problem is ‘stiff’, it uses the backward differentiation method.

Since the system does not have any damping, it will continuously oscillate when the initial condition is not in equilibrium. Figure 4 shows the phase portrait of the system (Strogatz, 1994). The amplitude of the velocity is about 0.2 m/s, while that of the displacement is 0.3 cm. The phase portrait does not show any spiral behavior, which means that the system does not have any damping. The center of the ellipse corresponds to the equilibrium configuration. For a different initial position, the radius of the ellipse will be changed. This observation is different from that of Post and Ryutov (1996), who showed that the system has negative damping-based linear perturbation. However, the numerical result in Figure 4 shows that the system does not have any energy-dissipating mechanism and is neutrally stable.

Theoretically, the levitation force can be increased proportionally to the velocity of the cradle. However, in practice, the levitation force is always limited by the weight of the cradle. When the velocity of the cradle is increased, the gap g_1 is also increased, so that the levitation force remains in the same magnitude. In addition, the gap will not increase continuously because the two side arrays generate a large counter-balance force in such a case. Figure 5 shows the levitation force and gap as a function of velocity of the cradle. From the

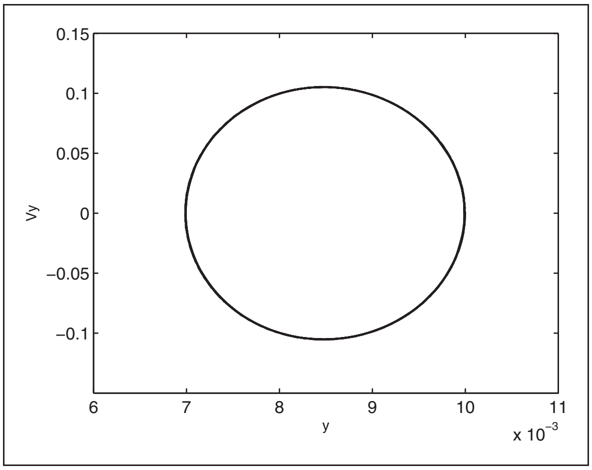

Figure 4. Phase portrait of the 1-DOF model between g_1 and v_y. The system is neutrally stable.

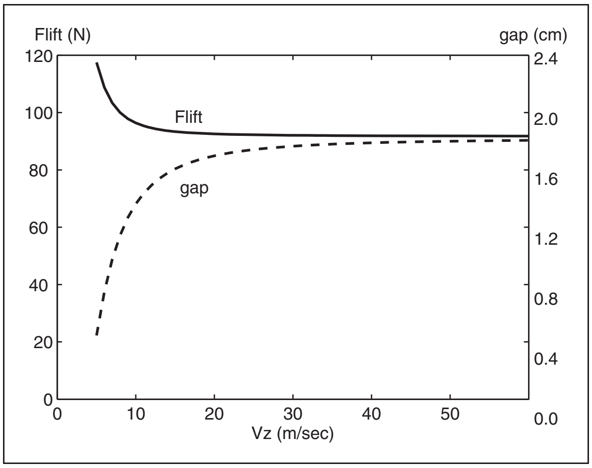

Figure 5. Change of levitation force and gap with respect to longitudinal velocity. Owing to the counter-balance force from the side arrays, both show a stable behavior.

figure, it can be concluded that the cradle shows a stable behavior in high velocity.

3.3. 2-DOF model

A 2-DOF model consists of the vertical and the longitudinal motions of the cradle. The cradle is considered as a lumped mass. The main purposes of this model are (1) to identify the unknown parameters, (2) to study the effect of magnetic drag force and the behavior of the cradle under variable velocities, and (3) to model the contact conditions between the track and the cradle using the compliant contact model with inelastic restitution as damping.

The configuration of the cradle is the same as with the 1-DOF model. Accordingly, the levitation force in Equation (18) can be used. In addition to F_y, there exists a drag force due to the motion of the cradle, which can be obtained from Equation (7) and the configuration of the cradle in Figure 3, as

$$F_{\text{drag}} = 2N_c \frac{B_0\phi_0}{2L} \frac{R/\omega L}{1+(R/\omega L)^2} \times \left[w_{\text{top}} e^{-kg_1} + 2w_{\text{side}} e^{-kg_2}\right]. \qquad (21)$$

By comparing Equation (21) with Equation (18), it can be easily found that the two side magnets compensate the levitation force, while they are accumulated directly to the drag force. Thus, the system has more drag and less levitation than that designed based on the flat magnets on the box-frame track, which is consistent with the experimental observation (Tung et al., 2001).

In order to overcome the drag force, a thrust force is applied to the cradle by providing the drive coils with impulsive current that is synchronized with the position of the cradle. In practice, three adjacent coils are simultaneously excited per magnet array in order to increase the thrust force. The thrust force in Equation (13) is obtained assuming that a single coil is excited when the magnetic field reaches its maximum value. A scalar variable β is included in order to consider the effect of three coils. Accordingly, the thrust force of the cradle in Figure 3 is given as

$$F_{\text{drive}} = 2\beta\left[w_{\text{top}} e^{-kg_1} + 2w_{\text{side}} e^{-kg_2}\right] \frac{2v_z}{\lambda} \frac{\tau}{\pi} I_D B_0. \qquad (22)$$

The thrust force is linearly proportional to the longitudinal velocity, whereas the drag force in Equation (21) is decreased once it reaches the maximum value at the transient velocity $\omega = R/L$. Thus, it is possible to find the velocity that makes the drag and thrust be in equilibrium. At that speed, the cradle will move with the constant speed.

Before presenting the differential equation for the 2-DOF model, the method of imposing the contact constraint is first discussed. The magnetic arrays are not allowed to penetrate the track, which can be imposed using the following contact constraints:

$$\begin{aligned} g_1(t) &\geq 0 \\ g_2(t) &\geq 0. \end{aligned} \qquad (23)$$

A Lagrange multiplier or a penalty method can be used to impose the unilateral boundary condition in the differential equation (Haug, 1989). When the Lagrange multiplier method is applied to the variational principle, the governing equation becomes a differential-algebraic equation, and an additional variable is added to the system. The advantage of this method is that it can impose the contact constraint exactly, and the Lagrange multiplier corresponds to the contact force. When the penalty method is used, however, no additional variable is added to the original differential equation. If the contact condition is violated, then it is penalized using a large penalty parameter.

In practice, the contact interface between two flexible bodies shows compliant behavior due to the local deformation (Hunt and Crossley, 1975). In addition, the restitution is not fully elastic. In this paper, the compliant contact model with inelastic restitution as damping is used to impose the contact condition. The differential equation of the dynamic problem with the penalized contact constraint becomes

$$\begin{aligned} ma_y &= F_{\text{lift}}(v_z, g_1) - F_{\text{cont}}(g_1, \dot{g}_1) - \sqrt{2}F_{\text{cont}}(g_2, \dot{g}_2) - ma_g \\ ma_z &= F_{\text{drive}}(v_z, g_1) - F_{\text{drag}}(v_z, g_1), \end{aligned} \tag{24}$$

where $F_{\text{cont}}(g, \dot{g})$ is defined as

$$F_{\text{cont}}(g, \dot{g}) = \begin{cases} kg + b\dot{g} & \text{if } g < 0 \\ 0 & \text{otherwise} \end{cases}, \tag{25}$$

where k and b are, respectively, the stiffness and damping coefficients of the contact interface. The contact force for the two side arrays is applied in the direction normal to the 45° inclined surface, and only the vertical component is considered. The above ordinary differential equation is solved with the following initial conditions:

$$\begin{aligned} y(0) = y_0, &\quad v_y(0) = v_{y0} \\ z(0) = z_0, &\quad v_z(0) = v_{z0}\,. \end{aligned} \tag{26}$$

The second-order differential equations can now be converted to the system of first-order differential equations, as

$$\dot{\mathbf{q}} = \begin{Bmatrix} \dot{y} \\ \dot{v}_y \\ \dot{z} \\ \dot{v}_z \end{Bmatrix} = \begin{Bmatrix} v_y \\ [F_{\text{lift}} - F_{\text{cont}}(g_1, \dot{g}_1) \\ -\sqrt{2}F_{\text{cont}}(g_2, \dot{g}_2)]/m - a_g \\ v_z \\ \left(F_{\text{drive}} - F_{\text{drag}}\right)/m \end{Bmatrix}. \tag{27}$$

Table 2. Results from the parameter identification. The shape parameter is reduced from its ideal value, while the equivalent thrust parameter is increased

Parameters	Initial value	Optimum value
α	1	0.7295
β	3	3.9298
$f(\alpha, \beta)$	1.5622	0.0427

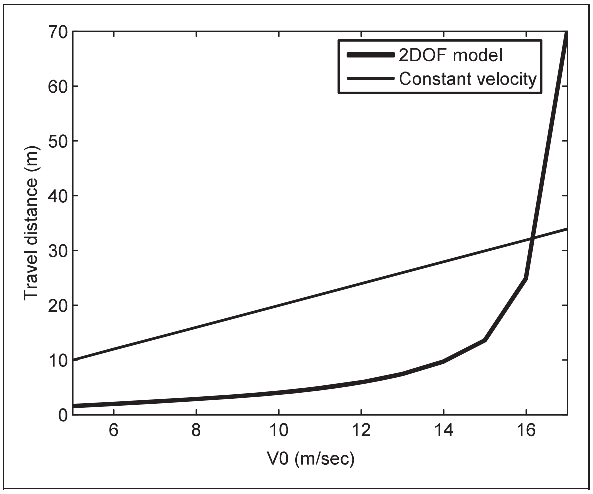

Figure 6. Travel distance for the first 2 seconds with respect to the initial velocity. The velocity increases after the critical velocity 18.5 m/s.

Before the numerical simulation of the 2-DOF model, the unknown parameters, α and β, need to be identified. For that purpose, the test results performed by Tung et al. (2001) are utilized. The maximum traveling distances for different initial velocities are first measured. The difference between these distances and those from the dynamic analysis is minimized by changing the two parameters. The design identification problem can then be written as

$$\text{Minimize } f(\alpha, \beta) = \sqrt{\sum_{i=1}^{4} \left(d_i^{\text{test}} - d_i^{\text{simulation}}\right)^2}. \tag{28}$$

The above minimization problem is solved using MATLAB 'fminsearch' function. The initial values are chosen from their ideal cases. Table 2 shows the initial and optimum values of the parameters. As expected, the shape parameter α is reduced from its ideal values, while β is increased. At the optimized values of the parameters, the error function $f(\alpha, \beta)$ is reduced significantly.

Figure 6 shows the traveling distance during the first 2 seconds with respect to various initial velocities. For comparison purposes, the travel distance with constant velocity is also plotted. When the initial velocity is less than the critical velocity ($v_0 = 16.2\,\text{m/s}$), the velocity decreases and the cradle eventually stops. At the critical velocity, the cradle moves with a constant velocity. The

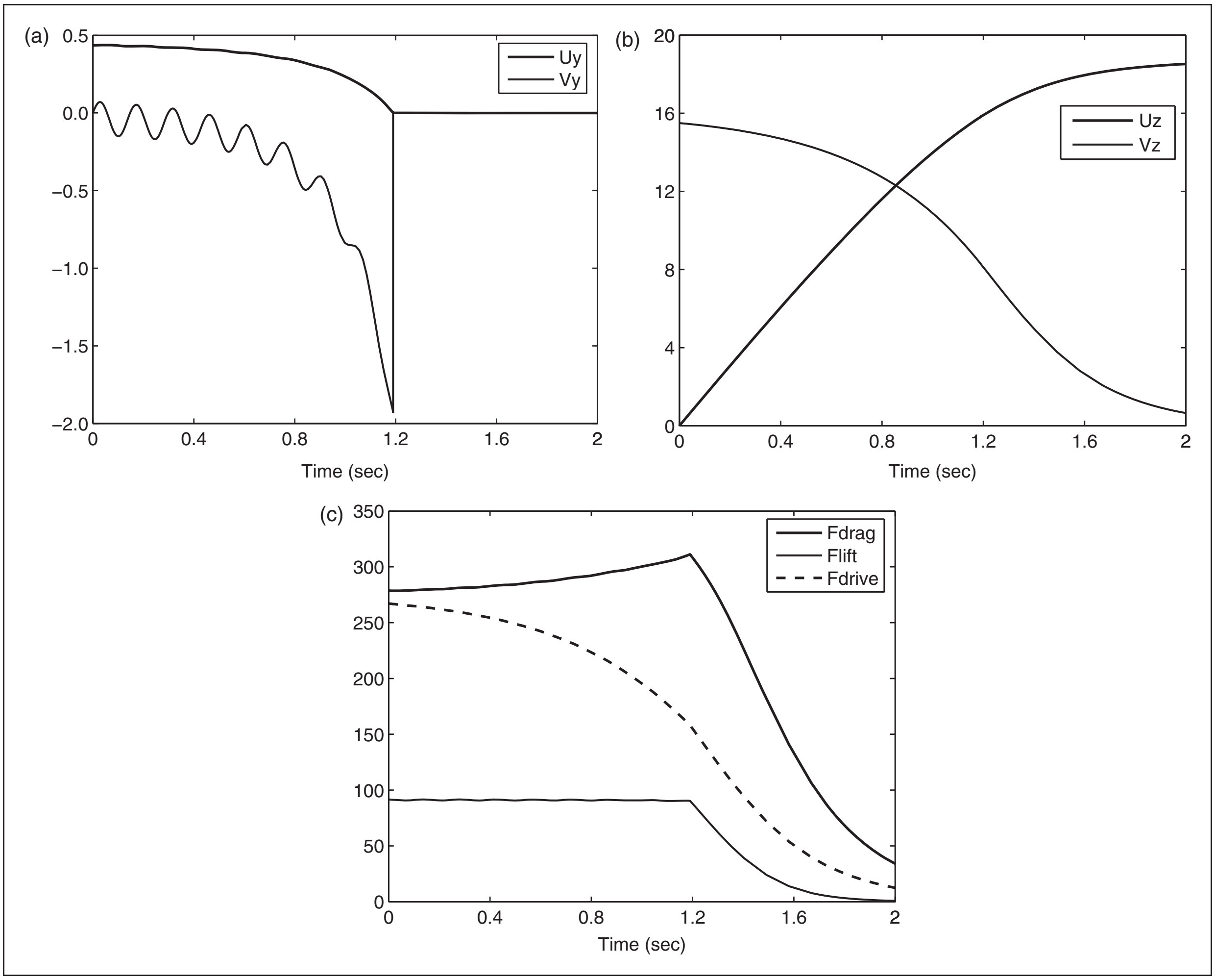

Figure 7. Dynamic analysis results for the 2-DOF model. (a) Vertical position (cm) and velocity (cm/s). (b) Traveling distance (m) and velocity (m/s). (c) Drag, lift, and thrust forces (N).

velocity increases exponentially when the initial velocity is above the critical value.

In order to evaluate the performance of the contact condition and the effect of the drag force, the two-DOF model is tested with the initial velocity $v_0 = 15.5\,\text{m/s}$. The initial velocity is chosen to be less than the critical velocity, so that the cradle touches the track as the velocity is reduced. Figure 7(a) shows the vertical position and velocity of the cradle. The vertical velocity shows a small oscillatory behavior, while the vertical position shows a stable behavior. The cradle touches the track at time = 1.19 seconds and slides on the track. Since the compliant contact force in Equation (25) is applied when the vertical position is negative, the vertical position shows a small penetration of 0.01 mm when the cradle stays on the track. The amount of penetration will be reduced as the contact stiffness is increased.

Figure 7(b) shows the traveling distance and velocity of the cradle. Since the initial velocity is less than the critical velocity, the velocity is reduced monotonically until the cradle stops. At time = 2 seconds, the cradle is still moving on the track, even if it slows down. The cradle eventually stops at time = 3 seconds.

Figure 7(c) shows the drag, lift, and thrust forces. As explained in the 1-DOF model, the lift force remains almost constant in the lifting region. The drag force is about three times larger than the lift force in the most lifting regions, and it is slightly increased even if the velocity is reduced. This is different from Figure 2, where the lift force is larger than the drag force. This is due to the effect of side arrays that compensate the lift force. Once the cradle touches the track, the drag and lift forces are reduced quickly. The drive force shows a similar trend with that of the velocity.

In general, the 2-DOF model shows a stable behavior. When the velocity is above the critical velocity, the vehicle is continuously lifted and the velocity is increased. In practice, the velocity can be controlled by changing the impulsive current in the drive coils.

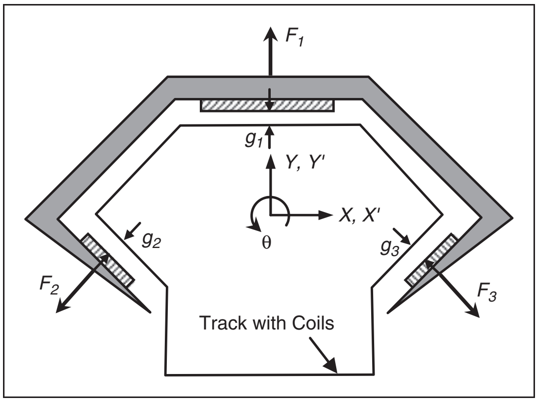

Figure 8. Four-DOF Inductrack dynamic model. The *X–Y* coordinate is fixed on the track, while the *X'–Y'* coordinate is fixed on the cradle.

When the velocity is reduced, the vehicle lands on the track and eventually stops.

3.4. 4-DOF model

In 1- and 2-DOF models, the cradle is assumed to be a lumped mass structure. The purpose of the 4-DOF model is to evaluate the rigid body behavior of the system. The cradle can move in the *z*-direction (thrust), *y*-direction (lift), *x*-direction (slip), and rotate in the *z*-direction (roll). Figure 8 shows the computational model with coordinate systems. The global coordinate *X–Y* is fixed on the track, while the local coordinate *X'–Y'* is fixed on the cradle. Both local and global coordinates have the same origin when the three magnets have the same gap (1.0 cm) with respect to the track. In order to simplify the contact calculation, the geometry of the magnets is represented by a point. In addition, it is assumed that the direction of the lift force is always normal to the track, not to the magnets. The effect of this assumption is not significant because the roll angle θ is supposed to be small.

The magnetic force depends on the gap between the magnets and the induced coils. The location of the magnets is calculated based on the local-to-global coordinate transformation. When the local coordinate of the magnet array *i* is given as $\mathbf{r}'_i$, the global coordinate can be obtained from

$$\mathbf{r}_i = \mathbf{r}_0 + \mathbf{A}(\theta) \cdot \mathbf{r}'_i, \quad i = 1, 2, 3, \tag{29}$$

where $\mathbf{r}_0 = (x, y)$ is the position of the origin of the local coordinate, and $\mathbf{A}(\theta)$ is the rotational transformation matrix defined as

$$\mathbf{A}(\theta) = \begin{bmatrix} \cos\theta & -\sin\theta \\ \sin\theta & \cos\theta \end{bmatrix}. \tag{30}$$

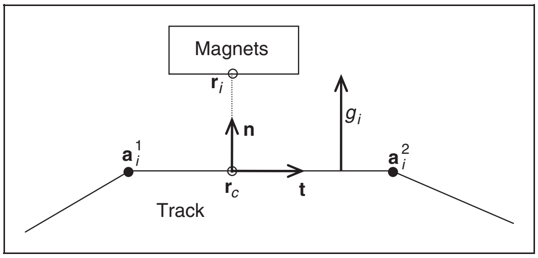

Figure 9. Contact condition between magnets and track. The magnets are considered as a point. The gap g_i must be non-negative.

First, the locations of three magnets are calculated from the geometry of the cradle in the local coordinate, and then, their global coordinates are calculated from Equation (29).

After calculating the global coordinate of the magnets, the gap between the magnets and the track can be calculated from the geometric relation. In order to make the procedure general, a concept from solid mechanics is adopted (Kim et al., 2000). Let $\mathbf{r}_i$ be the location of the magnet array *i*, and $\mathbf{a}_i^1$ and $\mathbf{a}_i^2$ be the coordinates of two end points of the track (see Figure 9). The segment of the track below the magnets is a straight line. The two end points are ordered such that the magnets should be on the left side when we go from $\mathbf{a}_i^1$ to $\mathbf{a}_i^2$. If the magnets are on the right side, it is considered that they penetrate the track and the contact force is applied to push them out. First, the unit tangent and normal vector to the track can be obtained by

$$\mathbf{t}_i = \frac{\mathbf{a}_i^2 - \mathbf{a}_i^1}{\|\mathbf{a}_i^2 - \mathbf{a}_i^1\|}, \quad \mathbf{n}_i = \mathbf{e}_3 \times \mathbf{t}_i, \tag{31}$$

where $\mathbf{e}_3$ is the unit vector in the *z*-coordinate, i.e. (0, 0, 1). Then, the gap between magnets and track can be calculated from

$$g_i = \left(\mathbf{r}_i - \mathbf{a}_i^1\right) \cdot \mathbf{n}_i \geq 0. \tag{32}$$

In addition, the rate of gap distance can be calculated by differentiating the relation in Equation (29) and using the property that the track is fixed, as

$$\dot{g}_i = \left(\mathbf{v}_0 + \dot{\mathbf{A}}(\theta) \cdot \mathbf{r}'_i\right) \cdot \mathbf{n}_i, \tag{33}$$

where

$$\dot{\mathbf{A}}(\theta) = \omega_z \begin{bmatrix} -\sin\theta & -\cos\theta \\ \cos\theta & -\sin\theta \end{bmatrix}. \tag{34}$$

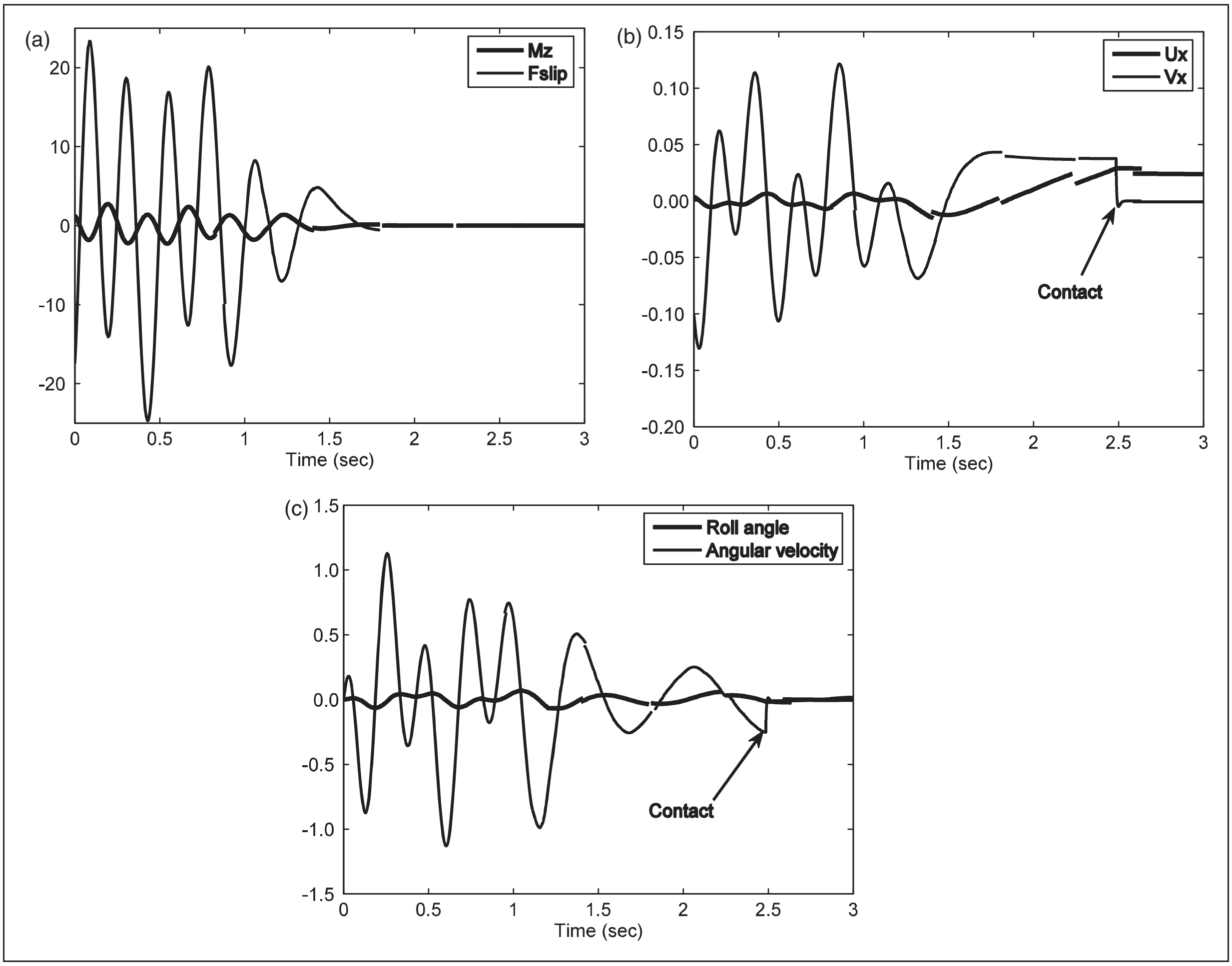

Figure 10. Slip and angular motions of the 4–DOF Inductrack model. (a) Moment (N-m) and slip force (N). (b) Lateral displacement (m) and velocity (m/s). The second magnet array contacts with the track at time = 2.5 s. (c) Roll angle (rad) and angular velocity (rad/s).

When these three magnets move along the track, they induce the flux in the coils. In the 4-DOF model, the peak flux can be obtained by

$$\phi_0 = \frac{\alpha B_0}{k}\sum_{i=1}^{3} w_i e^{-kg_i}. \tag{35}$$

As with the 2-DOF model, the shape parameter α is included. Then, the repulsive force at each magnet array can be written as

$$F_i = w_i e^{-kg_i}\frac{B_0\phi_0}{2L}\frac{2N_c}{1+(R/\omega L)^2} - F_{\text{cont}}(g_i, \dot{g}_i),\ i = 1, 2, 3. \tag{36}$$

These three repulsive forces, as illustrated in Figure 8, contribute to the lift and slip force of the cradle. Since it is assumed that these forces are applied in the direction normal to the track, the lift and slip forces can be obtained as

$$\begin{aligned} F_{\text{lift}} &= F_1 - (F_2 + F_3)\cos(45^\circ) \\ F_{\text{slip}} &= (F_3 - F_2)\sin(45^\circ). \end{aligned} \tag{37}$$

Different from the lift and slip forces in Equation (37), the drag force is obtained by adding the contribution from the three magnet arrays, as

$$F_{\text{drag}} = \sum_{i=1}^{3} w_i e^{-kg_i} \times 2N_c \frac{B_0\phi_0}{2L}\frac{R/\omega L}{1+(R/\omega L)^2}. \tag{38}$$

In order to overcome this drag force, the thrust force is applied to the cradle by providing impulsive current to the driving coils. Similar to the 2-DOF model, the thrust force can be obtained as

$$F_{\text{drive}} = 2\beta \sum_{i=1}^{3} w_i e^{-kg_i} \frac{2v_z}{\lambda} \frac{\tau}{\pi} I_D B_0, \tag{39}$$

where the parameter β is obtained using the optimization technique in Equation (28).

The dynamic model of the 4-DOF model includes lift, slip, thrust, and roll motions:

$$\begin{aligned} ma_x &= F_{\text{slip}} \\ ma_y &= F_{\text{lift}} - ma_g \\ ma_z &= F_{\text{drive}} - F_{\text{drag}} \\ I_{zz}\dot{\omega}_z &= M_z, \end{aligned} \tag{40}$$

where I_{zz} is the mass moment of inertia with respect to the z-coordinate and $\dot{\omega}_z$ is the angular acceleration in the roll motion. Note that the contact forces are included in the repulsive force in Equation (36).

The above ODE is solved with the following initial conditions:

$$\begin{aligned} x(0) &= x_0, \quad & v_x(0) &= v_{x0} \\ y(0) &= y_0, \quad & v_y(0) &= v_{y0} \\ z(0) &= z_0, \quad & v_z(0) &= v_{z0} \\ \theta(0) &= \theta_0, \quad & \omega_z(0) &= \omega_{z0}. \end{aligned} \tag{41}$$

The second-order differential equation can now be converted to the system of first-order differential equations, as

$$\dot{\mathbf{q}} = \begin{Bmatrix} \dot{x} \\ \dot{v}_x \\ \dot{y} \\ \dot{v}_y \\ \dot{z} \\ \dot{v}_z \\ \dot{\theta} \\ \dot{\omega}_z \end{Bmatrix} = \begin{Bmatrix} v_x \\ F_{\text{slip}}/m \\ v_y \\ F_{\text{lift}}/m - a_g \\ v_z \\ (F_{\text{drive}} - F_{\text{drag}})/m \\ \omega_z \\ M_z/I_{zz} \end{Bmatrix}. \tag{42}$$

The 4-DOF model is tested using the same initial conditions as those of the 2-DOF model. Initial conditions in the slip and roll motions are set to be zero, so that the same results as with the 2-DOF model can be obtained. The dynamic analysis results turn out to be identical to those of the 2-DOF model with numerical precision.

In order to test the response of the system under the slip and roll motions, a dynamic analysis is performed. The initial conditions are given such that the vehicle is perturbed in the lateral direction by $x_0 = 4\,\text{mm}$, $v_{x0} = -0.1\,\text{m/s}$, . All other initial conditions are the same as with 2-DOF model.

Figure 10 shows the slip and angular motions of the vehicle. The lifting and traveling motions of the vehicle are similar to those of the two-DOF model. The initial slip motion generates the lateral force F_{slip} and rolling moment M_z (Figure 10(a)). The vehicle contacts with the track at time = 2.5 seconds, when the slip velocity suddenly changes (Figure 10(b)). The initial slip motion induces a rolling motion as shown in Figure 10(c). However, the magnitudes of the rolling angle and the angular velocity are small.

4. Conclusions and future plans

The dynamic characteristics of an electromagnetic suspension system are evaluated using 1-DOF, 2-DOF, and 4-DOF numerical models. The dynamic model includes compliant contact constraints between the vehicle and the track. The unknown numerical parameters are identified using an optimization technique. Using a 1-DOF model, although the suspension system does not have any inherent damping in the lifting direction, a stable behavior is observed in the traveling direction; the vehicle is lifted when the velocity is above the threshold and lands on the track when the velocity is below the threshold. The 4-DOF model shows that the system has a strong concentric force that stabilizes the vehicle in the slip motion as well as in the rolling motion. Even if the levitation of the system can be achieved in the passive way, the system requires a thrust force in order to reach a large enough initial speed and maintain it against the drag force.

In the practical application of the electromagnetic suspension system, the vehicle has its own damping behavior due to the flexibility of the structure. This may explain the difference between the model test and the full-scale test. In order to model the damping characteristics of the structure, it is necessary to use the flexible-body dynamics model.

Funding

This work was supported in part by the Florida Space Grant Consortium sponsored by NASA Kennedy Space Center.

References

Boeij JD, Steinbuch M and Gutierrez HM (2005) Mathematical model of the 5-DOF sled dynamics of an electrodynamic maglev system with a passive sled. *IEEE Transactions on Magnetics* 41: 460–465.

Dill J and Meeker D (2000) *Maglifter Tradeoff Study and Subscale System Demonstration*. National Aeronautics and Space Administration (NASA), Hampton, Virginia.

Halbach K (1985) Application of permanent magnets in accelerators and electron storage rings. *Journal of Applied Physics* 57: 3605–3608.

Haug EJ (1989) *Computer-Aided Kinematics and Dynamics of Mechanical Systems. Volume 1: Basic Methods*. Boston, MA: Allyn and Bacon.

Hunt KH and Crossley FRE (1975) Coefficient of restitution interpreted as damping in vibroimpact. *Applied Mechanics* 42: 440–445.

Kalsi SS (1994) Superconductive electromagnetic suspension for Grumman maglev concept. In: Groom NJ (ed.) *Second International Symposium on Magnetic Suspension Technology Part 1*. Hapton: NASA, pp.197–211.

Kim NH, Choi KK, Chen JS and Park YH (2000) Meshless shape design sensitivity analysis and optimization for contact problems with friction. *Computational Mechanics* 25: 157–168.

Luerkin RF (1994) Transrapid (the first high-speed maglev train system certified and ready for application): Development status and prospect for development. In: Groom NJ (ed.) *Second International Symposium on Magnetic Suspension Technology Part 1*. Hapton: NASA, pp.77–91.

Matsue H, Demachi K and Miya K (2001) Numerical analysis of the superconducting magnet outer vessel of a maglev train by a structural and electromagnetic coupling method. *Physica C Superconductivity* 357–360: 874–877.

Post RF and Ryutov DD (1996) *Inductrack Concept: A New Approach to Magnetic Levitation*. Lawrence Livermore National Laboratory, Livermore.

Post RF and Ryutov DD (2000) The Inductrack: a simpler approach to magnetic levitation. *IEEE Transactions on Applied Superconductivity* 10: 901–904.

Powell JR and Danby GR (1971) Magnetic suspension for levitated tracked vehicle. *Cryogenics* 11: 192–204.

Rote DM and Cai Y (2002) Review of dynamic stability of repulsive-force maglev suspension systems. *IEEE Transactions on Magnetics* 38: 1383–1390.

Strogatz SH (1994) *Nonlinear Dynamics and Chaos: With Applications to Physics, Biology, Chemistry, and Engineering*. New York: Addison-Wesley.

Tung LS, Post RF and Martinez-Frias J (2001) *Final Progress Report for the NASA Inductrack Model Rocket launcher at the Lawrence Livermore National Laboratory*. Lawrence Livermore National Laboratory, Livermore.